UC Irvine
UC Irvine Previously Published Works

Title
Generation of bright isolated attosecond soft X-ray pulses driven by multicycle midinfrared lasers

Permalink
https://escholarship.org/uc/item/94b4j7hp

Journal
Proceedings of the National Academy of Sciences of the United States of America, 111(23)

ISSN
0027-8424

Authors
Chen, MC
Mancuso, C
Hernańdez-García, C
et al.

Publication Date
2014-06-10

DOI
10.1073/pnas.1407421111

Copyright Information
This work is made available under the terms of a Creative Commons Attribution License, availalbe at https://creativecommons.org/licenses/by/4.0/

Peer reviewed

eScholarship.org Powered by the California Digital Library
University of California

Generation of bright isolated attosecond soft X-ray pulses driven by multicycle midinfrared lasers

Ming-Chang Chen[a,b], Christopher Mancuso[a], Carlos Hernández-García[a,c], Franklin Dollar[a], Ben Galloway[a], Dimitar Popmintchev[a], Pei-Chi Huang[b], Barry Walker[d], Luis Plaja[c], Agnieszka A. Jaroń-Becker[a], Andreas Becker[a], Margaret M. Murnane[a,1], Henry C. Kapteyn[a,1], and Tenio Popmintchev[a]

[a]JILA and Department of Physics, University of Colorado Boulder, Boulder, CO 80309-0440; [b]Institute of Photonics Technologies, National Tsing Hua University, Hsinchu 30013, Taiwan; [c]Grupo de Investigación en Óptica Extrema, Universidad de Salamanca, E-37008 Salamanca, Spain; and [d]Department of Physics, University of Delaware, Newark, DE 19716

Contributed by Margaret M. Murnane, April 24, 2014 (sent for review April 3, 2014)

High harmonic generation driven by femtosecond lasers makes it possible to capture the fastest dynamics in molecules and materials. However, to date the shortest subfemtosecond (attosecond, 10^{-18} s) pulses have been produced only in the extreme UV region of the spectrum below 100 eV, which limits the range of materials and molecular systems that can be explored. Here we experimentally demonstrate a remarkable convergence of physics: when midinfrared lasers are used to drive high harmonic generation, the conditions for optimal bright, soft X-ray generation naturally coincide with the generation of isolated attosecond pulses. The temporal window over which phase matching occurs shrinks rapidly with increasing driving laser wavelength, to the extent that bright isolated attosecond pulses are the norm for 2-μm driving lasers. Harnessing this realization, we experimentally demonstrate the generation of isolated soft X-ray attosecond pulses at photon energies up to 180 eV for the first time, to our knowledge, with a transform limit of 35 attoseconds (*as*), and a predicted linear chirp of 300 *as*. Most surprisingly, advanced theory shows that in contrast with *as* pulse generation in the extreme UV, long-duration, 10-cycle, driving laser pulses are required to generate isolated soft X-ray bursts efficiently, to mitigate group velocity walk-off between the laser and the X-ray fields that otherwise limit the conversion efficiency. Our work demonstrates a clear and straightforward approach for robustly generating bright isolated attosecond pulses of electromagnetic radiation throughout the soft X-ray region of the spectrum.

ultrafast | coherent | nonlinear optics

High-order harmonic generation (HHG) is the most extreme nonlinear optical process in nature, making it possible to coherently upconvert intense femtosecond laser light to much shorter wavelengths (1, 2). High harmonics are radiated as a result of a coherent electron recollision process that occurs each half-cycle of the driving laser field while an atom is undergoing strong-field ionization. The short pulse duration of HHG (which must be shorter than the driving laser pulse) has made it possible to directly access the fastest timescales relevant to electron dynamics in atoms, molecules, and materials. The unique properties of attosecond HHG in the extreme UV (EUV) have uncovered new understanding of fundamental processes in atoms, molecules, plasmas, and materials, including the timescales on which electrons are emitted from atoms (3), the timescale for spin–spin and electron–electron interactions (4, 5), the timescale that determines molecular dissociation and electron localization (6–9), the timescale and mechanisms for spin and energy transport in nanosystems (10–12), as well as new capabilities to implement EUV microscopes with wavelength-limited spatial resolution (13).

The temporal structure of HHG is related to the number of times a high-energy electron undergoes a coherent recollision process, as well as the time window over which bright harmonics emerge. Using multicycle 0.8-μm driving lasers, HHG generally emerges as a train of attosecond (*as*) pulses (14, 15) corresponding to a series of harmonic peaks in frequency space. This emission can narrow to a single isolated *as* burst when the driving laser field is a few optical cycles (~5 fs) in duration (16, 17), with an associated broad continuous spectrum. Other techniques can isolate a single burst using a combination of multicolor fields and polarization control (18–26) or spatial lighthouse gating of the driving laser pulses (27, 28). Phase matching can also result in bright isolated *as* pulse generation for short driving laser pulses (29, 30). To obtain bright, phase-matched, high harmonic beams, the laser and HHG fields must both propagate at the speed of light c so that emission from many atoms interferes constructively. Above a critical ionization level, the phase velocity of the laser exceeds c, which terminates the HHG temporal emission. The chirp present on attosecond bursts can be compensated by using thin materials, gases, or chirped mirrors (31–33). To date, however, most schemes for creating isolated attosecond pulses require either very short-duration few-cycle 0.8-μm driving laser pulses that are difficult to reliably generate, or complex polarization modulation schemes. In addition, the carrier envelope phase (CEP) of the driving laser pulse must be stabilized.

A more general understanding of how to efficiently sculpt the temporal, spatial, and spectral characteristics of HHG emission over an extremely broad photon energy range (from the EUV to the keV and higher) has emerged in recent years (34–39). This understanding is critical both for a fundamental understanding of strong-field quantum physics, as well as for applications which have fundamentally different needs in terms of the HHG pulse

Significance

Attosecond pulses driven by femtosecond lasers make it possible to capture the fastest electron dynamics in molecules and materials. To date, attosecond pulses driven by widely available 800-nm lasers were limited to the extreme UV region of the spectrum, which restricted the range of materials, liquid, and molecular systems that could be explored because of the limited penetrating power. Our recent work showed that longer-wavelength midinfrared driving lasers at wavelengths from 1 to 4 μm are optimal for generating shorter-wavelength, bright, soft X-ray beams. Here we show that longer-pulse-duration midinfrared lasers are also optimal for generating shorter-pulse-duration, attosecond, soft X-rays. This is an unexpected and beautiful convergence of physics: bright, soft X-ray high harmonics naturally emerge as isolated attosecond bursts.

Author contributions: M.-C.C., C.M., M.M.M., and H.C.K. designed research; M.-C.C., C.M., C.H.-G., F.D., B.G., D.P., P.-C.H., B.W., L.P., A.A.J.-B., A.B., M.M.M., H.C.K., and T.P. performed research; M.M.M. and H.C.K. contributed new reagents/analytic tools; M.-C.C., C.M., C.H.-G., F.D., B.G., A.A.J.-B., A.B., M.M.M., H.C.K., and T.P. analyzed data; and M.-C.C., C.M., C.H.-G., F.D., L.P., A.A.J.-B., A.B., M.M.M., H.C.K., and T.P. wrote the paper.

The authors declare no conflict of interest.

Freely available online through the PNAS open access option.

[1]To whom correspondence may be addressed. E-mail: murnane@jila.colorado.edu or Kapteyn@jila.colorado.edu.

duration, spectral bandwidth, and flux. By considering both the microscopic single-atom response as well as the macroscopic coherent buildup of HHG, efficient phase-matched HHG can now be implemented from the EUV to >keV photon energies, simply by driving HHG with midinfrared (mid-IR) femtosecond driving lasers. This advance represents, to our knowledge, the first general-purpose, tabletop, coherent soft X-ray light source (39). Furthermore, theory suggested that bright isolated attosecond X-ray bursts would be achievable using multicycle mid-IR driving lasers in a phase-matched geometry (35). However, the low repetition rate of the driving lasers precluded experimental testing of these predictions. Moreover, formidable computation requirements meant that advanced simulations could not be fully extended into the mid-IR region at 2–4 μm.

In this paper, we experimentally demonstrate a beautiful convergence of physics for mid-IR (2-μm) driving lasers by showing that the conditions for optimal bright, soft X-ray generation naturally coincide with the generation of bright isolated attosecond soft X-ray bursts. We combine advanced theory with a novel experimental method equivalent to high-resolution Fourier transform spectroscopy to measure bright, attosecond soft X-ray pulses for the first time, to our knowledge. Specifically, we measure a field autocorrelation pulse width of 70 *as*, corresponding to a transform-limited 35-*as* pulse, that is supported by a coherent supercontinuum spectrum extending to photon energies around 180 eV. We also validate experimentally, for the first time, to our knowledge, the most intuitive dynamic picture of phase matching of HHG in the time domain by clearly demonstrating that the temporal window during which phase matching occurs shrinks rapidly with increasing driving laser wavelength. Finally, we show through advanced theory that the isolated attosecond pulse is chirped to 300 *as*. Most surprisingly, we find that bright attosecond pulse generation in the soft X-ray region requires the use of longer-duration, multicycle, mid-IR driving lasers to mitigate group velocity walk-off issues that would otherwise reduce the conversion efficiency. By harnessing the beautiful physics of phase matching, this work represents the simplest and most robust scheme for attosecond soft X-ray pulse generation, and will make attosecond science and technology accessible to a broader community.

Experiment

In our experiment, laser pulses at wavelengths of 0.8, 1.3, and 2.0 μm are generated using a 1-kHz Ti:sapphire laser pumping a three-stage optical parametric amplifier (OPA). The pulse durations at all three wavelengths were adjusted to be ∼10 cycles in duration (24 fs at 0.8 μm – 9.5 cycles, 35 fs at 1.3 μm – 8 cycles, and 90 fs at 2.0 μm – 13.5 cycles) and were measured using second-harmonic frequency-resolved optical gating. Each driving laser beam was focused into a 2-mm-long, Ar-filled cell, as shown in Fig. 1. The laser peak intensity at the focus was estimated by measuring the maximum HHG photon energy and then using the single-atom cutoff rule $(I \cdot \lambda_L^2)$ (40, 41). The lens was translated to precisely control the focal position and obtain optimal phase matching (42). (See *Methods* for more details.)

To characterize isolated subfemtosecond pulses, we implemented a soft X-ray Fourier transform field autocorrelation because it is the most straightforward and unambiguous way to distinguish an isolated *as* X-ray pulse from a train of pulses. Moreover, it has the added advantage of extremely high spectral resolution, so that we can unambiguously measure a true continuous spectral supercontinuum that is required to support an isolated attosecond pulse in the time domain. The X-ray field autocorrelation trace $A_F(\tau)$ is given by

$$A_F(\tau) = \int_{-\infty}^{\infty} |E_{\text{X-ray}}(t) + E_{\text{X-ray}}(t-\tau)|^2 dt$$
$$= 2 \cdot \int_{-\infty}^{\infty} |E_{\text{X-ray}}(t)|^2 dt + 2 \cdot Re \int_{-\infty}^{\infty} E^*_{\text{X-ray}}(t) E_{\text{X-ray}}(t-\tau) dt, \quad [1]$$

where $E_{\text{X-ray}}(\tau)$ represents the complex X-ray electric field. This field autocorrelation $A_F(\tau)$ directly measures the number of attosecond bursts in the HHG pulse train. Although the widely used alternate attosecond streaking technique (43) directly measures the laser field, it gives indirect information about the number of X-ray bursts in the train because of the lack of suitable atoms with strong X-ray absorption cross-sections over a very broad bandwidth, the unknown phase dependence of the transition dipole matrix in ionization, and the poor signal-to-noise levels of current measurement.

In our experiment, the HHG beam was refocused using a Kirkpatrick–Baez mirror pair. Two replicas of the HHG beam were then obtained by using an in-line, partially-split-mirror, spatial beam separator that can delay a part of the HHG beam with respect to itself with ultrahigh temporal resolution of ∼1.5 *as* (Fig. 1). A precise field autocorrelation of the HHG pulse was measured by monitoring the resultant fringes using an X-ray CCD (Andor). A Fourier transformation of the field autocorrelation yields a very high resolution power spectrum, which is in very good agreement with the experimentally measured spectrum (Fig. 2).

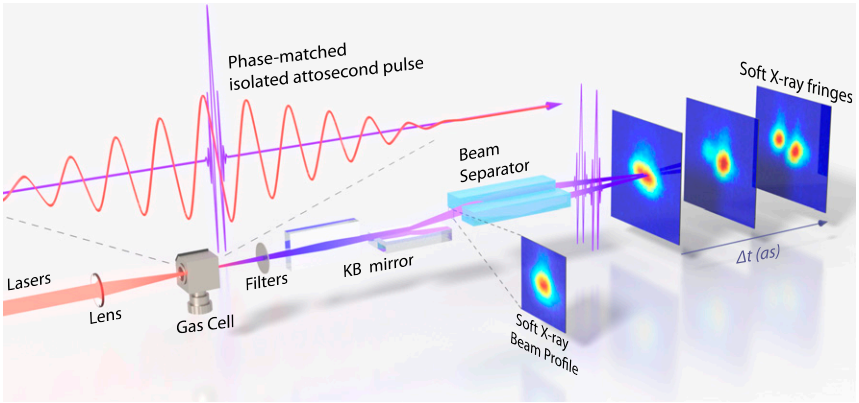

Fig. 1. Schematic of the setup for attosecond high-resolution Fourier transform spectroscopy. The number of discrete bursts in an attosecond pulse train driven by 0.8-, 1.3-, and 2.0-μm lasers is directly measured using soft X-ray interferometry, by delaying one part of the HHG pulse with respect to itself with ultrahigh precision of 1.5 *as*.

Note that the spectral resolution of the retrieved spectrum is determined by the maximum time-delay range of the field autocorrelator (300 fs), and is 0.01 eV. Although the temporal profile (chirp) of the individual attosecond X-ray pulses cannot be determined from a field autocorrelation, it enables the most precise determination of how many attosecond bursts are emitted, because a total of $2n-1$ fringes will be measured if there are n attosecond bursts in the pulse train.

Fig. 2 plots the experimental HHG field autocorrelations and their corresponding Fourier transforms at low and high laser intensity conditions for 0.8-, 1.3-, and 2-μm 10-cycle FWHM laser fields. (High laser intensity corresponds to optimal phase matching at the highest photon energies possible in Ar, and generating the brightest HHG flux.) When driving the HHG process with a 0.8-μm laser, we observe that the number of X-ray bursts decreases (from 15 to 9) as the driving laser intensity is increased (from 1.5×10^{14} to 2.6×10^{14} W/cm^2). For the case of a 1.3-μm driving laser, the number of individual bursts decreases faster (from 9 to 4 bursts as the laser intensity is increased from 1.3×10^{14} to 2.1×10^{14} W/cm^2). Finally, for a 2-μm driving laser, we obtain a remarkable result: the number of individual harmonic bursts decreases to a single isolated burst as the driving laser intensity reaches 1.6×10^{14} W/cm^2. Moreover, the HHG flux increases with increasing laser intensity. For 2-μm driving lasers in particular, the HHG emission shifts to a central photon energy of 140 eV (spanning from 90 to 180 eV), with a FWHM bandwidth of ~60 eV capable of supporting an ~35-*as* transform-limited pulse. This pulse duration is corroborated by the measured 70-*as* field autocorrelation trace, which, as expected, corresponds to twice the transform-limited pulse duration of 35 *as*. As discussed in more detail below, although the single isolated burst is predicted to be linearly chirped to ~300-*as* duration, it nevertheless represents, to our knowledge, the highest photon energy, broadest bandwidth, isolated *as* pulse characterized to date (26). Moreover, both the number of individual HHG bursts and the spectrum are insensitive to the phase of the laser carrier wave with respect to the pulse envelope (CEP), which was verified by adjusting the CEP of the 2-μm laser, as suggested by earlier experiments using 0.8-μm driving lasers (29, 30).

The high laser intensity used to obtain the data plotted in Fig. 2 is selected to access the phase-matching photon energy limits in Ar for each driving laser wavelength for 10-cycle laser pulses (~50 eV for 0.8 μm, 95 eV for 1.3 μm, and 175 eV for 2 μm; *Methods*). As discussed in detail below, phase matching is supported only during a narrow temporal window within the laser pulse. On the leading edge of the laser pulse, the laser phase velocity is $<c$ (speed of light), due to the dominance of neutral atoms. In contrast, on the trailing edge, the laser phase velocity is $>c$ due to ionization of the gas beyond the critical ionization level, which terminates phase matching (35). In the case of mid-IR driving lasers, three factors lead to a much shorter phase-matching window compared with 0.8-μm lasers: the harmonic order is higher, the period of the driving wave is longer, and the phase-matching pressure and ionization density are higher. Each of these factors contributes to a larger phase shift within each half-cycle and, therefore, to a shorter phase-matching window (Fig. 3). In contrast, for laser intensities below the critical ionization limit, optimal pressure and ionization are low, the harmonic order is low, and phase matching extends over many laser cycles. The practical consequence of this physical scaling is that for any driving laser wavelength, the temporal phase-matching window can be narrowed by increasing the driving laser intensity

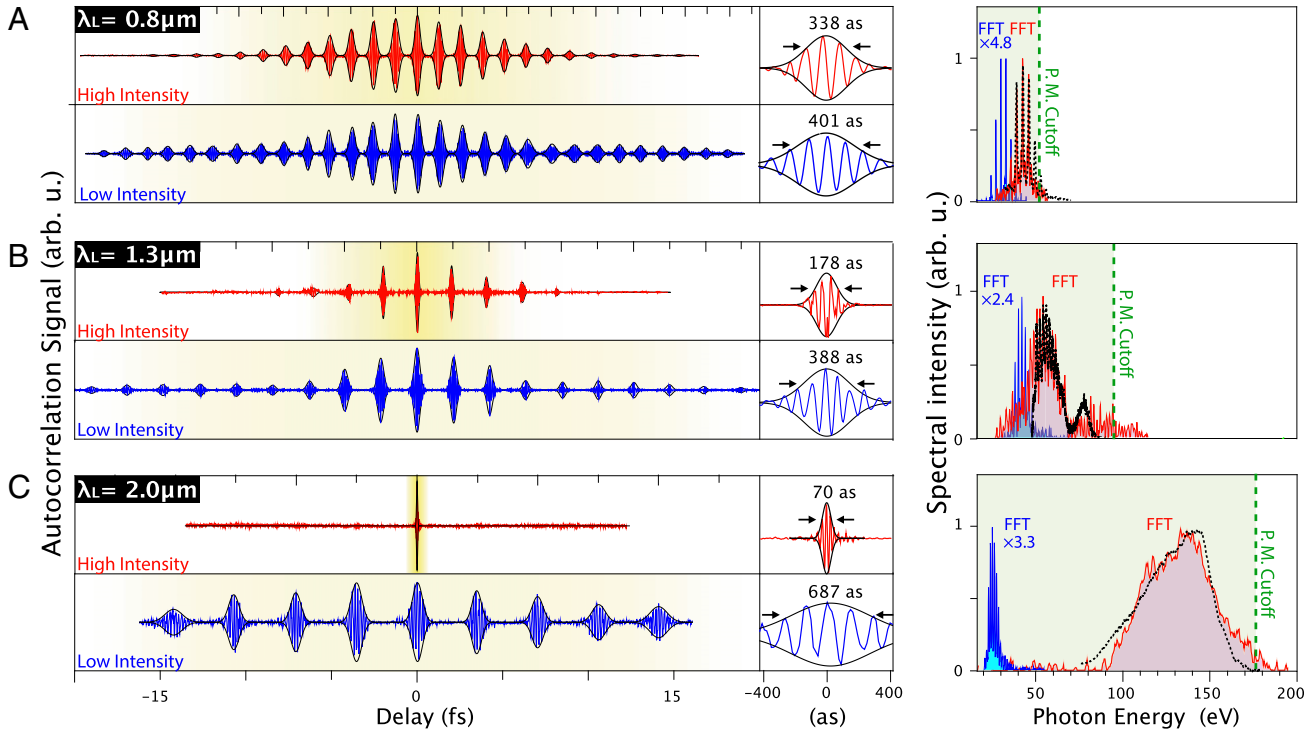

Fig. 2. Comparison of the experimental HHG autocorrelation data (normalized) from Ar driven by ~10 cycle laser pulses at wavelengths of (*A*) 0.8 μm, (*B*) 1.3 μm, and (*C*) 2 μm for high and low laser intensity conditions (red and blue lines). (*Left*) Field autocorrelation of the HHG field and enlarged view near time 0 with the coherence time of the central pulse envelope. The temporal phase-matching window is highlighted in yellow. Note that the bandwidth-limited pulse duration is half of this coherence time. (*Right*) HHG spectra obtained from the FFT of the field autocorrelation traces (filled-area plots), showing excellent agreement with the experimental spectra (black dotted lines). The low-intensity spectra are enhanced to see their fine structure. The predicted phase-matching cutoffs are also shown (green dashed lines).

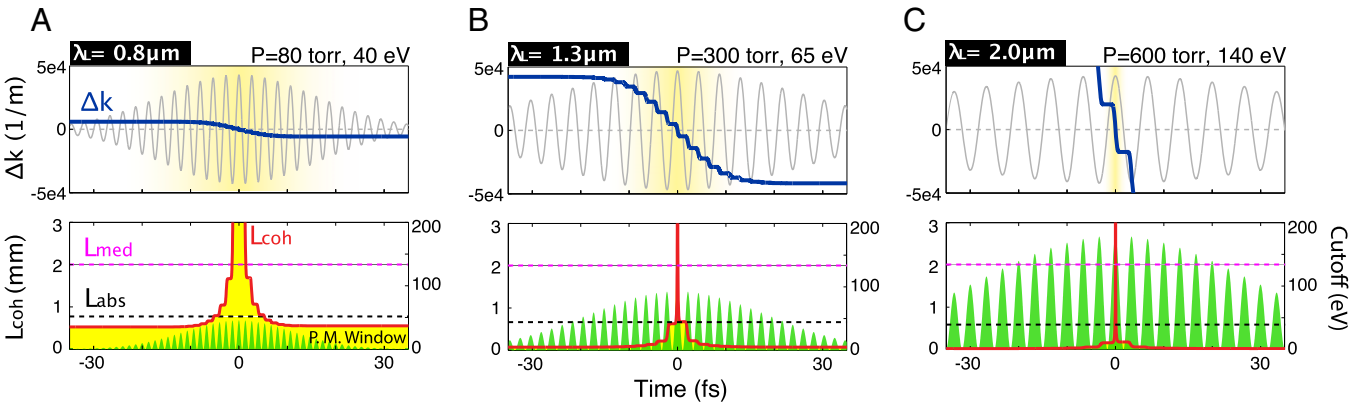

Fig. 3. Calculated phase mismatch Δk (blue line), L_{coh} (red line and yellow highlight), and instantaneous HHG cutoff photon energy (green) for HHG in Ar driven by 10-cycle laser pulses: (*A*) 0.8 μm, 2.42 × 10^{14} W/cm^2; (*B*) 1.3 μm, 1.87 × 10^{14} W/cm^2; and (*C*) 2.0 μm, 1.5 × 10^{14} W/cm^2. The temporal window during which phase matching occurs is highlighted in yellow.

and gas pressure. However, for longer driving laser wavelengths, the temporal narrowing effect is much stronger, so that isolated attosecond pulse generation is more robust and simple.

The flux of the HHG beam initially grows quadratically with pressure, but saturates at different pressures depending on the driving laser wavelengths and the absorption lengths (L_{abs}) in various regions of the spectrum. The general trend is that higher HHG photon energies require longer-wavelength mid-IR driving lasers and significantly higher pressure–length products for optimal conversion efficiency (35). Using a 0.8-μm driving laser, the brightest (phase-matched) HHG emission peaks at 40 eV, where the optimal backing pressure is 80 torr. However, for 1.3- and 2-μm driving lasers, the phase-matched peaks shift to 65 eV at 350 torr and 140 eV at 600 torr, respectively, with a photon flux of ∼10^{11} photons/s or ∼10^8 photons per shot (spanning from 90 to 180 eV). These optimized phase-matching pressures, observed experimentally, are all in excellent agreement with the predicted absorption-limited HHG emission for media lengths L_{med}∼$3L_{abs}$ (L_{med} = 2 mm; for Ar, L_{abs} = 0.81 mm at 40 eV, 0.67 mm at 65 eV, and 0.59 mm at 140 eV) (44, 45). Our approach thus supports the propagation and optimal growth of an isolated attosecond pulse in an extended high-pressure medium of millimeter to centimeter length scales, which is essential for efficient soft X-ray generation using mid-IR lasers.

We emphasize that the attosecond field autocorrelation demonstrated here is sufficient to understand and characterize how temporal gating of phase matching scales with driving laser wavelength, provided that the emission indeed exhibits coherence in the time domain from burst-to-burst. Such an assumption is consistent with all experimental studies of HHG to-date (14, 15). Moreover, the excellent experimentally measured spatial coherence of phase-matched HHG driven by mid-IR lasers also demonstrates temporal coherence across the entire beam (37, 39, 46). Furthermore, simulations indicate that even in the unphysical situation where successive attosecond bursts have significantly different chirp, the field autocorrelation would show signatures of multiple bursts and be detected using our approach. In contrast with attosecond streaking, the field autocorrelation trace can directly measure the number of attosecond bursts contained in the HHG emission, i.e., a total of $2n - 1$ fringes will be measured if there are n bursts in the pulse train, and this can be used for faster experimental feedback in optimization. The field autocorrelation approach is also significantly more rigorous than merely observing if the HHG spectrum measured using a grating spectrometer forms a discrete or continuous spectrum. A supercontinuum spectral structure does not necessarily imply the presence of an isolated X-ray burst, because the attainable resolving power of a grating spectrometer is strongly dependent on the number of grating grooves illuminated, the smallest slit width used, and aberrations induced by the optical elements in the system. In contrast, the fast Fourier transform (FFT)-generated spectrum from a field autocorrelation trace can provide much higher resolving power, which is given by the Heisenberg's uncertainty relation of ΔE (eV) = 4.1357/T (fs), where ΔE is the FFT spectral resolution and T represents the maximum temporal delay range. The delay range used in our HHG spatial beam separator was ∼300 fs, which supports an extremely high spectral resolution of ∼0.01 eV (much smaller than the energy spacing between individual harmonics of 0.62 eV). This capability for high-resolution spectral measurements is essential to resolve unambiguously whether the HHG spectrum is discrete or continuous in the case of a mid-IR driver, where the harmonic order can in some cases be as high as 5,000 (39). Finally, our attosecond field autocorrelation technique allows for direct probing of the temporal window during which phase matching is possible, thus experimentally validating our understanding of dynamic phase matching of HHG and its scaling with driving laser wavelength.

The alternative technique commonly used to measure attosecond pulses is attosecond streaking, where the attosecond field is first converted into an electron wavepacket through single-photon photoionization by the *as* pulse (43). If this photoionization occurs in the presence of an intense laser pulse, this laser field acts as an ultrafast electron phase modulator. A spectrometer can then measure the laser-field-modulated energy spectrum of this electron wavepacket, where the amplitude $a(v,\tau)$ of the electron wave function detected with momentum v and time delay τ between the X-ray and laser fields is given by

$$a(v,\tau) = -i\int_{-\infty}^{\infty} E_{X-ray}(t-\tau)\cdot d[v+A(t)] \cdot \exp\left\{ i\left[I_p\, t - 1/2\int_t^{\infty} p^2(t')\cdot dt' \right] \right\} dt, \qquad [2]$$

where $p(t) = v + A(t)$ is the instantaneous momentum of the free electron in the laser field, $A(t)$ is the vector potential from mid-IR pulses, $d[v]$ is the dipole transition matrix element from the ground state to the continuum state with momentum v, and I_p is the ionization potential of the atom. The resulting change in the width and offset of the photoelectron spectrum carries information about the pulse duration and the chirp of the attosecond pulse.

However, there are limitations to attosecond streaking for characterizing pulses in the soft X-ray regime. First, because this technique implements X-ray photoionization that generates an attosecond electron wavepacket in the continuum, the lack of suitable atoms that have strong X-ray absorption cross-sections over a broad bandwidth becomes a major challenge, especially in the case of mid-IR laser-driven HHG, where the phase-matched HHG bandwidth can be as broad as 1 keV. Second, the unknown phase dependence of the transition dipole matrix $d[\nu]$ on ν, as well as the influence of the ionic potential on the electron motion after ionization, could strongly influence the form of electron energy spectrum. Because these effects are not currently taken into account, attosecond streaking cannot as yet be guaranteed to provide the correct information about the attosecond pulse duration or the number of X-ray bursts in the train. Finally, to reconstruct the attosecond temporal bursts, one relies on sophisticated algorithms to decompose the attosecond bursts from a 2D data set (47, 48). Both the number of attosecond pulses and their duration is highly dependent on the data analysis—which is problematic given the usually poor signal-to-noise level of such measurements to date.

Theory

We use both an analytic theory and an advanced numerical model to understand why the phase-matching window shrinks rapidly with increasing driving laser wavelength and how phase matching scales with the driving laser pulse duration in the mid-IR. In our analytical theory, we neglect variations in the geometric contribution to phase mismatch, which in experiment can be minimized either using a laser confocal parameter much longer than the medium length, or a guided-wave configuration (35). Thus, the major contributions to the phase mismatch $\Delta k = (k_{q\omega} - qk_{\omega})$ are due to the pressure-dependent neutral and free-electron plasma dispersion terms that can be written as

$$\Delta k(t) \approx P \cdot q \cdot \left([1 - \eta(t)] \cdot \delta n \cdot \frac{2\pi}{\lambda_L} - \eta(t) \cdot N_{atm} \cdot r_e \cdot \lambda_L \right), \quad [3]$$

where P is the gas pressure, q is the harmonic order, $\eta(t)$ is the instantaneous ionization fraction, δn is the difference between the indices of refraction at the fundamental and harmonic wavelengths, λ_L is the central wavelength of the driving laser, N_{atm} is the number density of atoms at 1 atm, and r_e is the classical electron radius. From Eq. **3**, phase matching ($\Delta k = 0$) will occur at some time t when $\eta(t) = \eta_c = [(N_{atm}\, r_e\, \lambda_L^2/\delta n\, 2\pi) + 1]^{-1}$ and η_c is the critical ionization. If $\Delta k \neq 0$, the harmonic signal builds up over a shorter propagation distance, until the relative phase of the driving and harmonic fields is shifted by π radians. This defines the coherence length $L_{coh} = \pi/\Delta k$, or the distance over which the HHG fields add constructively.

Fig. 3 plots the phase mismatch and coherence length as a function of time during the laser pulse for different driving laser wavelengths (based on Eq. **3**), and assuming Ammosov–Delone–Krainov ionization rates (49). According to these predictions, the phase-matching temporal window shrinks rapidly with increasing driving laser wavelength. This can be understood from Eq. **3**: because Δk is proportional to the product of the pressure and harmonic order, in the mid-IR region of the spectrum the phase mismatch will be higher and the coherence length shorter for adjacent half-cycles near optimal phase matching. Efficient HHG emission also requires that the coherence length is larger than the medium length, and that the medium length is greater than the HHG reabsorption distance (L_{abs}) i.e., $L_{coh} > L_{med} > L_{abs}$ (44, 45). Under our experimental conditions, $L_{med} \sim 3L_{abs}$.

Note that in Fig. 3, the laser intensity is adjusted so that perfect phase matching occurs at the peak of the laser pulse, to ensure the highest photon energies and brightest isolated attosecond pulse generation. Moreover, the pressure is increased for optimal phase matching so that emission from several absorption lengths of the HHG light is possible. In general, the position of the phase-matching window along the laser pulse depends on both the laser intensity and wavelength, whereas the width of the phase-matching window depends on the pressure–length product. This temporal width determines the number of individual bursts in the attosecond pulse train, as well as the HHG conversion efficiency. As the driving laser intensity is increased further, the phase-matching window moves along the pulse front, whereas both the phase-matching energy and the width of the phase-matching window are nearly constant.

We can also analytically estimate the width of the phase-matching window by calculating the time dependence of phase mismatch Δk from Eq. **3**:

$$\begin{aligned} \frac{\partial \Delta k(\tau)}{\partial \tau} &\approx -P \cdot q \cdot \left[\delta n \cdot \frac{2\pi}{\lambda_L} + N_{atm} \cdot r_e \cdot \lambda_L \right] \cdot \frac{d\eta(\tau)}{d\tau} \\ &\propto P \cdot q \cdot \lambda_L \cdot \frac{d\eta(\tau)}{d\tau}, \end{aligned} \quad [4]$$

where τ represents time measured in cycles of the driving laser. Note the neutral gas dispersion contribution in Eq. **4** is negligible compared with the free-electron dispersion contribution, especially for long-wavelength driving lasers. At low laser intensities, the harmonic order q and $[d\eta(\tau)]/d\tau$ are small, which suppresses phase-matching gating, in agreement with the data of Fig. 2 (low-intensity autocorrelation). Near-optimal phase matching, the pressure P_{PM}, and the central harmonic order q_{PM} scale by the laser wavelength as $P_{PM} \propto \lambda_L^2$ and $q_{PM} \propto 1/2 \cdot \lambda_L^{2.7}$, as have been observed experimentally (35, 37, 39). The scaling of q_{PM} arises from two contributions: a factor of $1/2 \cdot \lambda_L^{1.7}$ because the central energy of the *as* burst is half the phase-matching cutoff (35), and an additional factor of λ_L from the fundamental laser photon energy. Thus, under optimal phase-matching conditions, Eq. **4** can be approximated by $[\partial \Delta k(\tau)]/\partial \tau \propto \lambda_L^{5.7} \cdot [d\eta(\tau)]/d\tau$, which scales strongly with the wavelength of driving laser. The combined effects of higher pressures needed for bright HHG emission, the resulting higher harmonic orders, and a stronger free-electron dispersion for long-wavelength driving lasers creates a large phase-mismatch jump between adjacent half-cycles of the driving laser. Note that the larger separation of the half-cycles of the driving laser further isolates the *as* bursts. Consequently, a longer-wavelength driving laser can much more easily induce strong phase-matching temporal gating (Fig. 2), i.e., a smaller perturbation away from optimal phase-matching conditions—for example by increasing laser intensity or gas pressure—will isolate a single attosecond soft X-ray burst more easily when using mid-IR driving lasers compared with Ti:sapphire driving lasers.

We also performed advanced 3D numerical macroscopic HHG simulations using the method presented in ref. 50. We discretize the gas medium into elementary radiators, and propagate the radiation of each of these sources to the detector,

$$E_j(r_d, t) = \frac{q_j s_d}{c^2 |r_d - r_j|} \left[s_d \times a_j \left(t - \frac{|r_d - r_j|}{c} \right) \right], \quad [5]$$

where q_j is the charge of the electron, s_d is the unitary vector pointing to the detector, and r_d and r_j are the position vectors of the detector and of the elementary radiator, respectively. The dipole acceleration a_j of each elementary source is computed using the SFA+ method, which is an extension of the standard strong-field approximation (SFA) (51). The signal at the detector is computed as the coherent addition of the HHG contributions of all of the elementary sources where the HHG light is assumed to propagate to the detector with a phase velocity c

(i.e., we discretize the gas medium into elementary radiators, and propagate the radiation of each of these sources to the far-field detector). Propagation effects of the fundamental field, including plasma and neutral dispersion as well as time-dependent group velocity walk-off, are all taken into account. The absorption of the harmonics in the gas is modeled using Beer's law, through a 2-mm argon gas cell of uniform density, at different pressures. The laser pulse was modeled in time as a Gaussian envelope, 8-cycle FWHM (53 fs), with peak intensity of 1.2×10^{14} W/cm^2, chosen to reach optimal phase-matching conditions ($\Delta k = 0$) at the center of the 2-μm–wavelength laser pulse.

To illustrate strong phase-matching temporal gating, as well as group velocity walk-off effects, Fig. 4 *A–F* compares the HHG emission as a function of pressure for single-cycle versus multicycle driving laser pulses (1.5-cycle and 8-cycle pulses, respectively). The electric field of the laser is plotted at the entrance and the exit of the cell. As the pressure is increased from 5 to 600 torr, the increasing contribution of the neutral atom dispersion induces a phase shift on the front of the pulse, whereas the presence of the free-electron plasma induces a chirp on the trailing edge of the pulse. The combined effect confines the phase-matching window to a suboptical cycle duration (300 *as*) in the center of the pulse, where a bright isolated linearly chirped attosecond pulse (group delay dispersion ~0.005 fs^2) is generated at high pressures. As the 2-μm driving laser pulse duration is reduced from 8 to 1.5 cycles, there is a strong contribution due to group velocity walk-off that leads to a temporal delay of the envelope of the laser field as it propagates (Fig. 4*C*). As a result, the phase-matching window completely disappears for 1.5-cycle driving lasers at high pressures, thus inhibiting bright isolated *as* pulse generation. This group velocity walk-off clearly is still present for an eight-cycle pulse, and the envelope of the pulse slightly lags the phase-matched half-cycle. However, near the peak of the pulse, this shift does not interfere with optimal phase matching (Fig. 4 *D–F*).

Finally, comparing HHG propagation for low and high pressures, for low pressures (5 torr) an attosecond pulse train is emitted, where the positive slope of the time–frequency structure (Fig. 4*G*) reveals the survival and phase matching of short trajectories after propagation. In the high-pressure case (600 torr), phase-matching temporal gating isolates a single attosecond burst from the previous train, over a time interval of ~300 *as* (Fig. 4*H*). The neutral- and free-electron dispersion cause the attosecond HHG fields generated both at the front and back of the laser pulse to interfere destructively. The phase-matched HHG bandwidth (~60 eV FWHM) of the isolated attosecond pulse supports a Fourier transform limit of ~35-*as* temporal duration, which agrees very well with our experimental observations.

In summary, we demonstrate a robust method for generating bright isolated attosecond soft X-ray pulses by exploiting the time-dependent phase-matching dynamics of HHG driven by multicycle mid-IR lasers. Using a soft X-ray autocorrelator with 1.5-*as* precision to directly and precisely count the number of individual attosecond bursts, we provide, to our knowledge, the first unambiguous experimental evidence for generating isolated attosecond pulses in the soft X-ray region. This direct measurement of the temporal structure of bright HHG also validates experimentally, to our knowledge, for the first time in the time domain, that phase matching involves a balance between time-dependent neutral atom and plasma dispersions, as well as the scaling of dynamic phase matching with laser wavelength. Surprisingly, we show that in contrast with *as* pulse generation in the EUV, long-duration, multicycle driving laser pulses are required to generate isolated soft X-ray bursts efficiently, to mitigate group velocity walk-off between the laser and the X-ray fields that otherwise limit the conversion efficiency. Moreover, this approach does not require

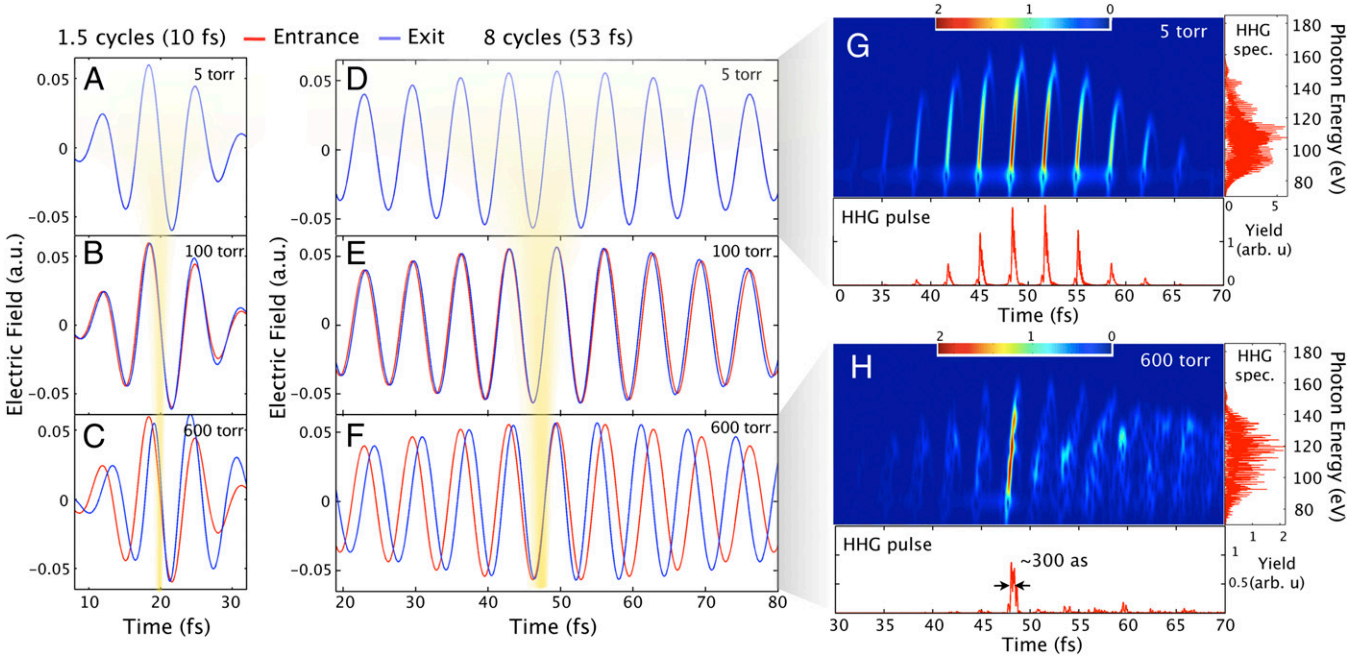

Fig. 4. Numerical calculations showing the dependence of the phase-matching window on the number of driving laser cycles of a 2-μm laser, and the gas pressure. The laser field is shown both at the entrance (red) and exit (blue) of a 2-mm gas cell at pressures of (*A* and *D*) 5 torr, (*B* and *E*) 100 torr, and (*C* and *F*) 600 torr for 1.5 cycles and 8 cycles FWHM at phase-matching intensities of 1.3×10^{14} W/cm^2 and 1.2×10^{14} W/cm^2, respectively, from the central part of a driving laser field with a Bessel profile of radius 60 μm. The time window during which phase matching is possible is highlighted in yellow. The temporal profile of the HHG emission from the eight-cycle laser field is shown for (*G*) 5 torr and (*H*) 600 torr. (*Right*) Time–frequency analysis together with the HHG spectrum and temporal emission, which evolves from an *as* pulse train (*G*) to an isolated 300-*as* chirped pulse (*H*). Note that for a 1.5-cycle driving laser, at the high pressures required for bright HHG emission, phase matching is not possible due to group velocity walk-off.

the use of few-cycle driving lasers with carrier envelope stabilization or other complex technologies. This new technique presents an accessible and reliable route to generate stable, isolated attosecond pulses in the keV region with pulse durations in the single-digit attosecond and even zeptosecond range (38, 39). This method is applicable to all technologies for mid-IR ultrashort pulse generation, including emerging new laser materials, parametric amplification techniques, optical fiber, or fiber-bulk lasers. Our results will expand the field of attosecond science, making it possible to capture the attosecond motion of electrons in a broader range of atoms, molecules, liquids, and materials.

Methods

Laser system: In our experiment, laser wavelengths of 1.3 and 2 μm are generated in a three-stage OPA seeded by a white-light continuum. The OPA is pumped by a 1-kHz, 23-fs Ti:sapphire laser amplifier system delivering pulse energies of up to 12 mJ, and operating at a central wavelength of 0.8 μm. To seed the OPA, a small part of the Ti:sapphire beam (~10 μJ) is used to generate a white-light continuum in a sapphire plate, which is then further chirped in time. A signal beam at 1.3 μm was amplified to ~100 μJ by overlapping the signal seed (1.3 μm) with the 0.8-μm pump pulse in time, and at the phase-matching angle of a beta-barium borate crystal. The resulting output energy was 2.5 mJ for the signal beam at 1.3 μm, and 1.6 mJ for the corresponding idler beam of 2 μm. A total conversion efficiency of 35% from the pump into both the signal and idler was achieved. The output stability of the OPA was less than 3% root-mean-square. We measured the pulse duration of 0.8-, 1.3-, and 2-μm beams using second harmonic frequency-resolved optical gating. To reach the HHG phase-matching laser intensity, these three wavelengths were focused using different focal length lens, resulting in the following focal parameters: Wavelength 0.8 μm; focal spot size 70 μm; confocal length 10 mm. Wavelength 1.3 μm; focal spot size 70 μm; confocal length 6 mm. Wavelength 2 μm; focal spot size 70 μm; confocal length 4 mm.

ACKNOWLEDGMENTS. The authors acknowledge help from B. Langdon and A. Auger. The authors acknowledge support from the Department of Energy Office of Basic Energy Sciences (Atomic, Molecular, and Optical Science Program) and facilities provided by a National Security Science and Technology Faculty Fellowship and the National Science Foundation (NSF) Center for Extreme Ultraviolet Science and Technology. M.-C.C. and P.-C.H. acknowledge support by Taiwan National Science Council (Grant 102WFA0400681). C.M. and B.G. gratefully acknowledge support from an NSF Graduate Research Fellowship and a National Nuclear Security Administration Stewardship Science Graduate Fellowship. C.H.-G. acknowledges support by a Marie Curie International Outgoing Fellowship within the European Union Seventh Framework Programme for Research and Technological Development, under Research Executive Agency Grant Agreement 328334. L.P. acknowledges support from Junta de Castilla y León (Project SA116U13). A.A.J.-B. was supported by grants from the US NSF (Awards PHY-1125844 and PHY-1068706). This work used the Janus supercomputer, which is supported by the NSF (Award CNS-0821794) and the University of Colorado Boulder. The Janus supercomputer is a joint effort of the University of Colorado Boulder, the University of Colorado Denver, and the National Center for Atmospheric Research. Janus is operated by the University of Colorado Boulder.

1. McPherson A, et al. (1987) Studies of multiphoton production of vacuum-ultraviolet radiation in the rare gases. *J Opt Soc Am B* 4(4):595–601.
2. Li XF, L'Huillier A, Ferray M, Lompré LA, Mainfray G (1989) Multiple-harmonic generation in rare gases at high laser intensity. *Phys Rev A* 39(11):5751–5761.
3. Klünder K, et al. (2011) Probing single-photon ionization on the attosecond time scale. *Phys Rev Lett* 106(14):143002.
4. Rudolf D, et al. (2012) Ultrafast magnetization enhancement in metallic multilayers driven by superdiffusive spin current. *Nat Commun* 3:1037.
5. Miaja-Avila L, et al. (2008) Direct measurement of core-level relaxation dynamics on a surface-adsorbate system. *Phys Rev Lett* 101(4):046101.
6. Kim KT, et al. (2012) Amplitude and phase reconstruction of electron wave packets for probing ultrafast photoionization dynamics. *Phys Rev Lett* 108(9):093001.
7. Gagnon E, et al. (2007) Soft X-ray-driven femtosecond molecular dynamics. *Science* 317(5843):1374–1378.
8. Li W, et al. (2010) Visualizing electron rearrangement in space and time during the transition from a molecule to atoms. *Proc Natl Acad Sci USA* 107(47):20219–20222.
9. Rohwer T, et al. (2011) Collapse of long-range charge order tracked by time-resolved photoemission at high momenta. *Nature* 471(7339):490–493.
10. Mathias S, et al. (2012) Probing the timescale of the exchange interaction in a ferromagnetic alloy. *Proc Natl Acad Sci USA* 109(13):4792–4797.
11. Turgut E, et al. (2013) Controlling the competition between optically induced ultrafast spin-flip scattering and spin transport in magnetic multilayers. *Phys Rev Lett* 110(19):197201.
12. Siemens ME, et al. (2010) Quasi-ballistic thermal transport from nanoscale interfaces observed using ultrafast coherent soft X-ray beams. *Nat Mater* 9(1):26–30.
13. Seaberg MD, et al. (2011) Ultrahigh 22 nm resolution coherent diffractive imaging using a desktop 13 nm high harmonic source. *Opt Express* 19(23):22470–22479.
14. Paul PM, et al. (2001) Observation of a train of attosecond pulses from high harmonic generation. *Science* 292(5522):1689–1692.
15. Nabekawa Y, Shimizu T, Furukawa Y, Takahashi EJ, Midorikawa K (2009) Interferometry of attosecond pulse trains in the extreme ultraviolet wavelength region. *Phys Rev Lett* 102(21):213904.
16. Christov IP, Murnane MM, Kapteyn HC (1997) High-harmonic generation of attosecond pulses in the "single-cycle" regime. *Phys Rev Lett* 78(7):1251–1254.
17. Goulielmakis E, et al. (2008) Single-cycle nonlinear optics. *Science* 320(5883):1614–1617.
18. Corkum PB, Burnett NH, Ivanov MY (1994) Subfemtosecond pulses. *Opt Lett* 19(22):1870–1872.
19. Sola IJ, et al. (2006) Controlling attosecond electron dynamics by phase-stabilized polarization gating. *Nat Phys* 2(5):319–322.
20. Sansone G, et al. (2006) Isolated single-cycle attosecond pulses. *Science* 314(5798):443–446.
21. Mashiko H, et al. (2008) Double optical gating of high-order harmonic generation with carrier-envelope phase stabilized lasers. *Phys Rev Lett* 100(10):103906.
22. Feng X, et al. (2009) Generation of isolated attosecond pulses with 20 to 28 femtosecond lasers. *Phys Rev Lett* 103(18):183901.
23. Calegari F, et al. (2009) Efficient continuum generation exceeding 200 eV by intense ultrashort two-color driver. *Opt Lett* 34(20):3125–3127.
24. Altucci C, et al. (2010) Interplay between group-delay-dispersion-induced polarization gating and ionization to generate isolated attosecond pulses from multicycle lasers. *Opt Lett* 35(16):2798–2800.
25. Takahashi EJ, Lan P, Mücke OD, Nabekawa Y, Midorikawa K (2010) Infrared two-color multicycle laser field synthesis for generating an intense attosecond pulse. *Phys Rev Lett* 104(23):233901.
26. Sansone G, Poletto L, Nisoli M (2011) High-energy attosecond light sources. *Nat Photonics* 5(11):655–663.
27. Wheeler JA, et al. (2012) Attosecond lighthouses from plasma mirrors. *Nat Photonics* 6(12):829–833.
28. Kim KT, et al. (2013) Photonic streaking of attosecond pulse trains. *Nat Photonics* 7(8):651–656.
29. Sandhu A, et al. (2006) Generation of sub-optical-cycle, carrier-envelope-phase—insensitive, extreme-UV pulses via nonlinear stabilization in a waveguide. *Phys Rev A* 74(6):061803-1–061803-4.
30. Thomann I, et al. (2009) Characterizing isolated attosecond pulses from hollow-core waveguides using multi-cycle driving pulses. *Opt Express* 17(6):4611–4633.
31. López-Martens R, et al. (2005) Amplitude and phase control of attosecond light pulses. *Phys Rev Lett* 94(3):033001.
32. Kim KT, et al. (2007) Self-compression of attosecond high-order harmonic pulses. *Phys Rev Lett* 99(22):223904.
33. Morlens A-S, et al. (2005) Compression of attosecond harmonic pulses by extreme-ultraviolet chirped mirrors. *Opt Lett* 30(12):1554–1556.
34. Popmintchev T, et al. (2008) Extended phase matching of high harmonics driven by mid-infrared light. *Opt Lett* 33(18):2128–2130.
35. Popmintchev T, et al. (2009) Phase matching of high harmonic generation in the soft and hard X-ray regions of the spectrum. *Proc Natl Acad Sci USA* 106(26):10516–10521.
36. Popmintchev TV, Chen M-C, Bahabad A, Murnane MM, Kapteyn HC (2010) Phase-matched Generation of Coherent Soft and Hard X-rays Using IR Lasers. Provisional United States Patent Application: 61,171,783 (2008), US Patent US8,462,824B2.
37. Chen MC, et al. (2010) Bright, coherent, ultrafast soft X-ray harmonics spanning the water window from a tabletop light source. *Phys Rev Lett* 105(17):173901.
38. Popmintchev T, Chen M-C, Arpin P, Murnane MM, Kapteyn HC (2010) The attosecond nonlinear optics of bright coherent X-ray generation. *Nat Photonics* 4(12):822–832.
39. Popmintchev T, et al. (2012) Bright coherent ultrahigh harmonics in the keV x-ray regime from mid-infrared femtosecond lasers. *Science* 336(6086):1287–1291.
40. L'Huillier A, Schafer K, Kulander K (1991) Theoretical aspects of intense field harmonic-generation. *J Phys At Mol Opt Phys* 24(15):3315–3341.
41. Corkum PB (1993) Plasma perspective on strong field multiphoton ionization. *Phys Rev Lett* 71(13):1994–1997.
42. Balcou P, Salières P, L'Huillier A, Lewenstein M (1997) Generalized phase-matching conditions for high harmonics: The role of field-gradient forces. *Phys Rev A* 55(4):3204–3210.
43. Itatani J, et al. (2002) Attosecond streak camera. *Phys Rev Lett* 88(17):173903.
44. Constant E, et al. (1999) Optimizing high harmonic generation in absorbing gases: Model and experiment. *Phys Rev Lett* 82(8):1668–1671.
45. Durfee CG III, et al. (1999) Phase matching of high-order harmonics in hollow waveguides. *Phys Rev Lett* 83(11):2187–2190.
46. Bartels RA, et al. (2002) Generation of spatially coherent light at extreme ultraviolet wavelengths. *Science* 297(5580):376–378.
47. Mairesse Y, Quéré F (2005) Frequency-resolved optical gating for complete reconstruction of attosecond bursts. *Phys Rev A* 71(1):011401-1–011401-4.
48. Thomann I, et al. (2008) Temporal characterization of attosecond wave forms in the sub-optical-cycle regime. *Phys Rev A* 78(1):011806-1–011806-4.
49. Ammosov M, Delone N, Krainov V (1986) Tunnel ionization of complex atoms and of atomic ions in an alternating electromagnetic field. *Sov Phys JETP* 64(6):1191–1194.
50. Hernandez-Garcia C, et al. (2010) High-order harmonic propagation in gases within the discrete dipole approximation. *Phys Rev A* 82(3):033432-1–033432-11.
51. Pérez-Hernández JA, Roso L, Plaja L (2009) Harmonic generation beyond the Strong-Field Approximation: The physics behind the short-wave-infrared scaling laws. *Opt Express* 17(12):9891–9903.